# Meteoroid Orbit Determination from HPLA Radar Data

Jared T. Blanchard<sup>a,\*</sup>, Nicolas Lee<sup>a</sup> and Sigrid Elschot<sup>a</sup>

<sup>a</sup>Space Environment and Satellite Systems Lab, 496 Lomita Mall, Stanford, CA 94305 United States

#### ARTICLE INFO

# Keywords: Meteors Radar Observations Orbit Determination

#### ABSTRACT

High-power large-aperture radars have revolutionized meteor science by allowing highly accurate position and velocity estimates to be made from meteor head echoes. This paper describes a new open-source software, MODA, for determining the heliocentric orbital parameters of these meteoroids. We compare MODA with other current methods, both analytical and numerical. We describe our modelling of third-body perturbations and atmospheric drag, as well as solar radiation pressure, which is not taken into account in other works. We verify MODA against results from the literature and use it to compute the orbits for two small particles observed by ALTAIR in 2008.

# 1. Introduction

Earth is constantly bombarded by a steady stream of dust and small particles; it is estimated that 100 billion meteoroids with mass greater than one microgram enter Earth's atmosphere each day. Trigo-Rodríguez (2019) describes in detail the chemical makeup and implications of this meteoroid flux, and Trigo-Rodríguez and Blum (2022) discusses how we can use meteoroid flux information to infer physical characteristics of comets. A meteor is the observable plasma formed by a meteoroid passing through the Earth's atmosphere. One way scientists classify meteoroids is by their orbit of origin. Many come from cometary orbits that stretch to the outer reaches of the solar system, while others come from asteroidal orbits localized in the inner solar system. Baggaley et al. (2007), Meisel et al. (2002a,b), and Weryk and Brown (2004) have even identified interstellar particles. However, as Hajduková and Kornoš (2020) assert, the orbital elements of meteoroids with higher heliocentric velocities are more sensitive to errors in the observed entry velocity and radiant position. Hajduková et al. (2020) studies this problem in detail for the case of identifying 10 interstellar meteoroids, as the error required to mischaracterize a near-parabolic orbit is not necessarily large. For 11 example, in their description of fireballs detected by the FRIPON automatic fireball detection network over western 12 Europa, Colas et al. (2020) determine that all the meteoroids with hyperbolic orbits have high errors and therefore 13 cannot be classified as interstellar. Recent efforts to determine meteoroid trajectories take uncertainties into account at each algorithmic step. Jansen-Sturgeon et al. (2020) pass states and covariances from line-of-sight measurements 15 through a least-squares algorithm to find a best fit trajectory with covariances. Peña-Asensio et al. (2021) describe the 16 Python 3D-FireTOC package that automates the process of inferring atmospheric trajectories and heliocentric orbits 17 from video recordings, quantifying the errors in each step. 18

While much of meteor science depends on optical measurements, radars have become valuable tools in observing and estimating the properties of meteors and meteoroids. High-power large-aperture (HPLA) radars have especially revolutionized the meteor science community, allowing for precise measurements of both the small, dense plasmas that surround the meteoroid, referred to as head echoes, and the extended trails behind the meteoroid, referred to as trails (Dyrud et al., 2005). The high sensitivity and precise range resolution of HPLAs yield highly accurate head echo position and velocity measurements as described by Janches et al. (2008). What's more, analysis of the scattering caused by head echoes can yield estimates of the meteoroid's physical parameters. Close et al. (2012), Drew et al. (2004), and Marshall et al. (2017) describe techniques for calculating the mass, radius, and bulk density of very small meteoroids from head echoes, which includes modeling the scattering characteristics of the dense plasma. Pecina (2016) gives an full derivation of the scattering relations relevant to meteor plasma. Relating the scattering to the ablation process that forms the plasma requires a model for determining the structure of meteoroids based on radar head echoes (Campbell-Brown and Close, 2007). An important component for understanding head echoes is determining the peak plasma density and plasma distribution, which can be used to extract meteoroid mass and density. Recent

19

20

22

23

24

25

27

28

29

<sup>\*</sup>Corresponding author

<sup>≦</sup> jared711@stanford.edu (J.T. Blanchard); nnlee@stanford.edu (N. Lee); sigridc@stanford.edu (S. Elschot)
ORCID(s): 0000-0002-1907-2835 (J.T. Blanchard)

improvements in particle-in-cell (PIC) simulations include adding a background magnetic field (Sugar et al., 2018, 2019).

Various radar techniques have been developed to extract high quality signal-to-noise ratio (SNR) data from head echoes and model the radar wave interaction with the plasma. Volz and Close (2012) showed how compressed sensing can be used to reconstruct sparse signals of meteors and Marshall and Close (2015) created a finite difference time domain model of meteor head echo scattering to estimate meteor size and density. Yet the radar specifications, including frequency and polarization, will strongly influence the meteoroid population that can be observed at any one site. Dyrud et al. (2008a,b) modelled the reflections of radar signals from various facilities off meteoroid head echoes to understand what meteoroid populations will be easiest to observe from each radar. Vertatschitsch et al. (2011) describe the polarization of radar head echo measurements to show that detectability is highly dependent on radar polarization, and that most meteoroids are fragmenting as they fall through the atmosphere. Current studies focus on head-trail interaction (Close et al., 2011), modeling the plasma turbulence present in the trails (Yee and Close, 2013) and extracting background ionospheric properties and neutral densities using head echo deceleration data (Li and Close, 2015, 2016) and ablation behavior (Limonta et al., 2020).

One example of an HPLA radar used to study meteors is the ALTAIR complex on the Kwajalein Atoll of the Marshall Islands. Brown et al. (2001) used ALTAIR data to identify new meteor showers as well as interstellar particles (ISPs). Loveland et al. (2011) compared different methods for determining range rates from chirped pulses, showing that the phase unwrapping method made possible by ALTAIR radar's dual-frequency capabilities can significantly reduce the uncertainty about the predicted range rates. Figure 1 shows an example of head echo and trail data as observed by ALTAIR in 2007.

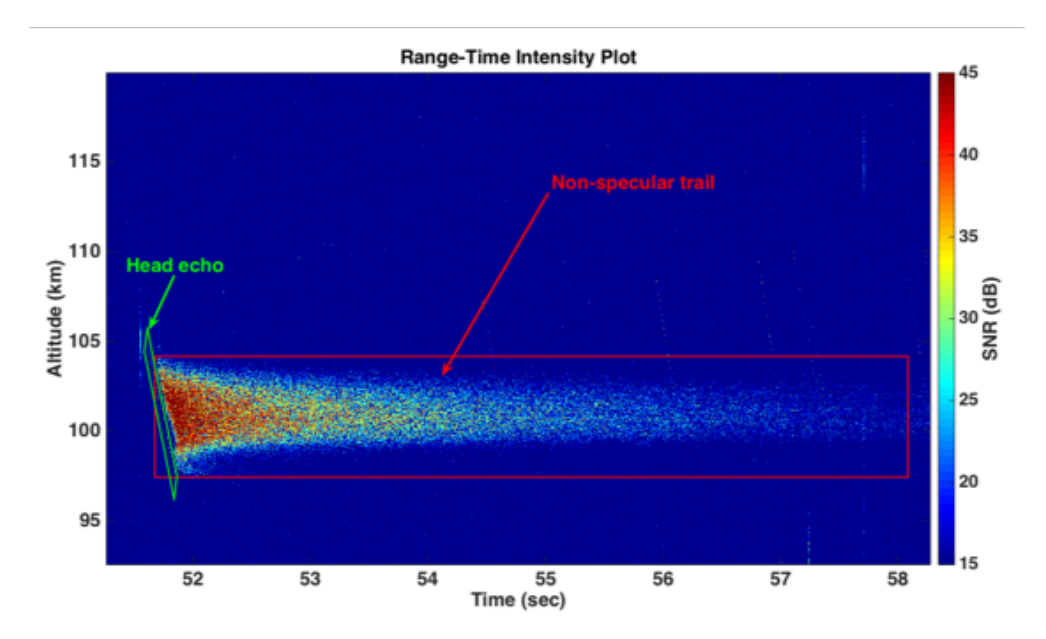


Figure 1: Range-time intensity plot of a nonspecular trail and head echo detected by ALTAIR in 2007.

When it comes to estimating the trajectory of a meteoroid through the atmosphere, and then determining its orbital parameters, much of the literature focuses on triangulating positions from multiple observation locations. Ceplecha (1987) developed a method that is used by most meteor and fireball groups to estimate orbital parameters from fish-eye photographs taken at two or more stations. His method assumes the meteor approaches Earth on a hyperbolic trajectory, analytically determining the asymptote according to two-body assumptions. He includes analytical adjustments to zenith angle and velocity that account for the effect of Earth's gravity and atmosphere on the meteoroid's trajectory. Zoladek (2011) created a multipurpose software tool in Python for the Polish Fireball Network and Langbroek (2004) developed an Excel spreadsheet for calculating meteor orbits, both based on Ceplecha's work. Jenniskens et al. (2011) use Ceplecha's method with some subtle corrections in their CAMS orbit software. The UFOOrbit software used by Kanamori (2009) to and the SPARVM software used by Christou and Atreya (2006) rely on input from the UFOCapture

3 E

software and use a similar analytical approach. Kozak (2008) developed a vector method, targeting TV observations of meteors, to determine the trajectory of a meteor in Earth's atmosphere and its heliocentric orbit elements. The recent work of Vida et al. (2020) gives details on the theory behind estimating meteor trajectories from optical measurements and the analytical equations used for frame conversions and corrections. Peña-Asensio et al. (2021) describe a comprehensive Python software package for performing meteor trace detection, trajectory reconstruction, and heliocentric orbit computation from optical recordings. Granvik and Brown (2018) analytically compute the heliocentric orbits for 25 meteorites and predict their escape routes from the main asteroid belt, while taking trajectory measurement uncertainty into account. They mention that the uncertainty in the velocity correction term is not well understood or documented in many published meteor studies, and could lead to significant differences in initial velocity.

More accurate analyses by Clark and Wiegert (2011) and Zuluaga et al. (2013) use numerical integration instead of the analytical correction techniques. Andersson (2018) uses the Python package REBOUND to backward-integrate meteoroids. The work of de la Fuente Marcos and de la Fuente Marcos (2013) uses backward integration with a Hermite integration scheme over hundreds of thousands of years to predict the origin of the Chelyabinsk superbolide. Dmitriev et al. (2015) added to their work by developing a numerical method that integrates a meteor orbit backward from its observed point to a point five million kilometers away, taking perturbations from the Moon, Sun, and planets into account. Their work resulted in a software tool for Windows called Meteor Toolkit that can compute a meteor's orbital parameters with standard deviations if given initial uncertainty measures on the observed initial state. Jansen-Sturgeon et al. (2019) compare Dmitriev's method of numerical integration and Ceplecha's analytical method with a novel numerical method that uses equinoctial orbital elements. They used the re-entry of the Hayabusa spacecraft, the orbit of which was known previously to high accuracy, to compare methods, showing a slight improvement of their method over Ceplecha's and Dmitriev's. Trigo-Rodríguez et al. (2015) computed the semi-major axis of the Annama meteoroid using the Spanish Meteor Network Software and Meteor Toolkit, with results within 6% of each other.

In this paper, we describe a new open-source tool that we developed for meteoroid orbit determination using MATLAB and JPL's SPICE toolkit (Acton, 1996). The tool, Meteoroid Orbit Determination Application (MODA), closely follows many of the same steps outlined in Dmitriev et al. (2015), but adds in the additional perturbation of solar radiation pressure (SRP) and integrates backward for much longer. MATLAB can be used on Windows, Linux, or Mac operating systems and offers flexibility in terms of loading in data. The code can be found at https://github.com/jared711/moda. As we will show later, the results from MODA agree well with the published results of the Meteor Toolkit.

# 2. HPLA Radar Data

High-power large-aperture (HPLA) radars can detect meteors passing through the beam at almost any angle with millisecond time resolution and spatial resolution of a few dozen meters according to Pellinen-Wannberg et al. (2008). The Advanced Research Projects Agency (ARPA) Long-Range Tracking and Instrumentation Radar (ALTAIR) is an HPLA radar facility in the Kwajalein Atoll with both UHF (422 MHz) and VHF (160 MHz) frequency capabilities. A monopulse feed system, it is capable of 3D position measurements with average accuracies of 11.2 mdeg for angles, 10 m for ranges, and 30 m/s for range rates (Close et al., 2002). ALTAIR transmits right-circularly (RC) polarized signals and receives both left-circular (LC) and right-circular polarization at receiver horns offset from the focus of the main 46 meter dish. The differences of the LC signal energies between receivers are used to measure the angle of arrival of the return signal. ALTAIR, shown in Figure 2, is located at 9.40°N and 167.48°E at 83.5 meters above sea level and has a peak power of 6 MW.

In this work, we use data collected from ALTAIR in 2007-2008. A VHF linear frequency modulated (LFM) chirped pulse with 100  $\mu$ s pulse width and a UHF LFM chirped pulse with a 400  $\mu$ s pulse width were used. The bandwidths were 7 MHz and 5 MHz for the VHF and UHF frequencies, respectively. The



Figure 2: The ALTAIR radar on Kwajalein Atoll, originally built to track spacecraft launches and deep space satellite orbits, serves as an important tool for meteor scientists (Hall et al., 2012).

pulse repetition interval (PRI) was 8.7 ms for both frequencies (Loveland et al., 2011). Figure 3 shows a typical distribution of meteor masses observed by ALTAIR during the 2007-2008 campaign, with a mean of about 10  $\mu$ g (Close et al. (2012)). Meteors of this size are classified as micrometeors and cannot be observed by the naked eye.

Meisel et al. (2002a) found that most interstellar meteoroids are micron-sized. These tiny meteoroids are observed at higher altitudes than their more massive counterparts and decelerate much more quickly due to atmospheric drag.

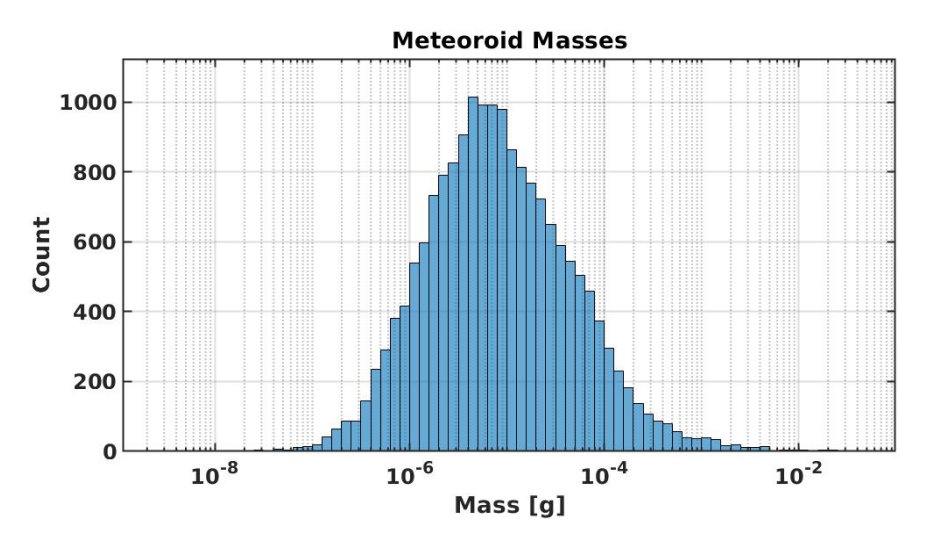


Figure 3: Distribution of meteoroid masses for a sample set detected by ALTAIR in 2007.

# 2.1. Data Processing

114

116

117

118

119

122

123

124

126

127

ALTAIR measures meteor head echoes as streaks that pass through the radar beam. Figure 4 shows examples of azimuth (relative to boresite) data obtained from ALTAIR along with fit lines and confidence intervals computed using least squares analysis. Similar streak plots exist for elevation (relative to boresite) and range as well. A line of best fit and the root mean squared error are computed for each streak. The rate terms  $\dot{r}$ ,  $\dot{\alpha}$ , and  $\dot{\beta}$  are assumed to be the slope of the line of best fit, and we use the 95% confidence interval of the slope parameter to compute standard deviations for the rate terms

$$\sigma_{\dot{r}} = \epsilon_{\dot{r},95\%}/4,\tag{1}$$

where  $\epsilon_{\dot{r},95\%}$  is the width of the 95% confidence interval of the slope parameter. Similar expressions are used for the  $\sigma_{\dot{\alpha}}$  and  $\sigma_{\dot{\beta}}$  terms.

# 3. Model

# 3.1. Spherical to Cartesian Coordinates

We begin with a radar measurement of the meteor in spherical coordinates: range r, azimuth  $\alpha$ , and elevation  $\beta$ . The velocity of the meteor is represented by the rates of change of the range, azimuth, and elevation represented as  $\dot{r}$ ,  $\dot{\alpha}$ , and  $\dot{\beta}$  respectively. The full state in spherical coordinates is written as

$$\mathbf{x}_{\text{sph}} = \begin{bmatrix} r, \ \alpha, \ \beta, \ \dot{r}, \ \dot{\alpha}, \ \dot{\beta} \end{bmatrix}^T. \tag{2}$$

Once we have a measurement corresponding to the meteor's state at the beginning of the streak, we convert from spherical to Cartesian coordinates, which is a nonlinear transformation. We introduce  $x_{ENU}$  to represent the Cartesian state vector (position and velocity) of the meteor relative to the radar in the East-North-Up (ENU) reference frame

$$\boldsymbol{x}_{\text{ENU}} = \begin{bmatrix} \boldsymbol{r}_{\text{ENU}} \\ \dot{\boldsymbol{r}}_{\text{ENU}} \end{bmatrix} = [\boldsymbol{x}_{\text{ENU}}, \ \boldsymbol{y}_{\text{ENU}}, \ \boldsymbol{z}_{\text{ENU}}, \ \dot{\boldsymbol{x}}_{\text{ENU}}, \ \dot{\boldsymbol{x}}_{\text{ENU}}]^T. \tag{3}$$

The transformation from  $x_{sph}$  to  $x_{ENU}$  is

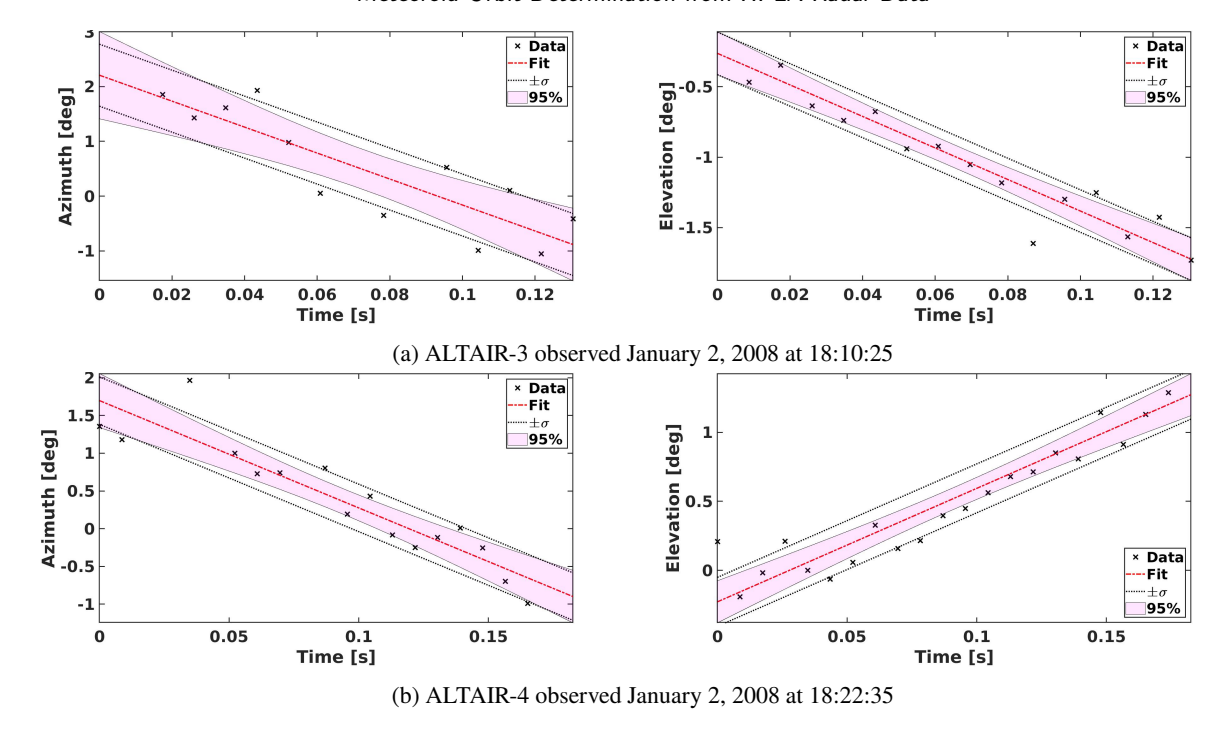


Figure 4: Azimuth and elevation (relative to boresite) evolution for two example meteor streaks obtained by ALTAIR. Black x's represent the actual data points while the red line is the line of best fit according to least-squares. Also shown is the standard deviation of the data (dotted black line) and the 95% confidence interval of the fit (magenta). The orbital elements of these meteoroids are found in Table 6.

Table 1 Frames of Reference

Acronym	Name	Type
ENU	East/North/Up	Rotating
ECEF	Earth-Centered, Earth-Fixed	Rotating
ECI	Earth-Centered Inertial	Inertial
SCI	Sun-Centered Inertial	Inertial

$$\mathbf{x}_{\text{ENU}} = f_1 \left( \mathbf{x}_{\text{sph}} \right) = \begin{bmatrix} r \cos \beta \sin \alpha \\ r \cos \beta \cos \alpha \\ r \sin \beta \\ \dot{r} \cos \beta \sin \alpha + r \dot{\alpha} \cos \beta \cos \alpha - r \dot{\beta} \sin \beta \sin \alpha \\ \dot{r} \cos \beta \cos \alpha - r \dot{\alpha} \cos \beta \sin \alpha - r \dot{\beta} \sin \beta \cos \alpha \\ \dot{r} \sin \beta + r \dot{\beta} \cos \beta \end{bmatrix}. \tag{4}$$

#### 3.2. Linear Frame Conversions

We must convert the state vector to a Sun-Centered Inertial (SCI) frame by going through the intermediate Earth-Centered, Earth-Fixed (ECEF) and Earth-Centered Inertial (ECI) frames shown in Figure 5 and Table 1.

### 3.2.1. ENU to ECEF

129

131

132

Since the ENU and ECEF frames are both fixed to the Earth, they rotate at the same rate, greatly simplifying the conversion. To perform the conversion we first need to know the position of the radar in the ECEF frame, given by

$$\mathbf{r}_{\text{ECEF}}^{\text{radar}} = \begin{bmatrix} (N+h)\cos\lambda\cos\phi \\ (N+h)\cos\lambda\sin\phi \\ (N(1-e_{\oplus}^2)+h)\sin\lambda \end{bmatrix}$$
 (5)

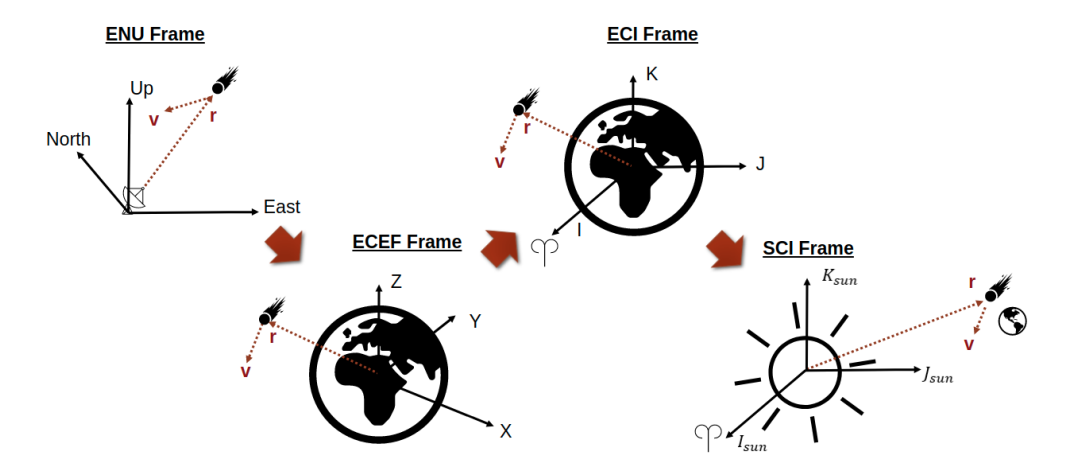


Figure 5: Illustration of position and velocity vectors representing the meteor state in each of four reference frames.

$$N = \frac{r_{\oplus}}{\sqrt{1 - e_{\oplus}^2 \sin^2 \lambda}} \tag{6}$$

where  $r_{\oplus} = 6,378.137$  km is the equatorial radius of the Earth,  $e_{\oplus} = 0.0818$  is the eccentricity of the Earth ellipsoid, h is the elevation of the radar above sea level, and  $\phi$  and  $\lambda$  are the geodetic latitude and longitude of the radar, respectively.

The frame conversion is written as

$$\mathbf{r}_{\text{ECEF}} = R_z(\pi/2 + \lambda)R_x(\pi/2 - \phi)\mathbf{r}_{\text{ENU}} + \mathbf{r}_{\text{ECFF}}^{\text{radar}} \tag{7}$$

$$\dot{\mathbf{r}}_{\text{ECEF}} = R_z(\pi/2 + \lambda)R_x(\pi/2 - \phi)\dot{\mathbf{r}}_{\text{ENU}},\tag{8}$$

which can be rewritten as an affine transformation in terms of the state vectors  $\mathbf{x}_{\text{ECEF}}$  and  $\mathbf{x}_{\text{ENU}}$ 

$$\boldsymbol{x}_{\text{ECEF}} = \begin{bmatrix} R_z(\pi/2 + \lambda)R_x(\pi/2 - \phi) & 0 \\ 0 & R_z(\pi/2 + \lambda)R_x(\pi/2 - \phi) \end{bmatrix} \boldsymbol{x}_{\text{ENU}} + \begin{bmatrix} \boldsymbol{r}_{\text{ECEF}} \\ 0 \end{bmatrix}. \tag{9}$$

Note that  $R_x(\cdot)$ ,  $R_y(\cdot)$ , and  $R_z(\cdot)$  are rotation matrices defined as

$$R_{x}(\theta) = \begin{bmatrix} 1 & 0 & 0 \\ 0 & \cos\theta & -\sin\theta \\ 0 & \sin\theta & \cos\theta \end{bmatrix}, \qquad R_{y}(\theta) = \begin{bmatrix} \cos\theta & 0 & \sin\theta \\ 0 & 1 & 0 \\ -\sin\theta & 0 & \cos\theta \end{bmatrix}, \qquad R_{z}(\theta) = \begin{bmatrix} \cos\theta & -\sin\theta & 0 \\ \sin\theta & \cos\theta & 0 \\ 0 & 0 & 1 \end{bmatrix}. \tag{10}$$

The time derivatives of these rotation matrices  $\dot{R}_x(\cdot)$ ,  $\dot{R}_v(\cdot)$ , and  $\dot{R}_z(\cdot)$  are

$$\dot{R}_{x}(\theta) = \dot{\theta} \begin{bmatrix} 0 & 0 & 0 \\ 0 & -\sin\theta & -\cos\theta \\ 0 & \cos\theta & -\sin\theta \end{bmatrix}, \quad \dot{R}_{y}(\theta) = \dot{\theta} \begin{bmatrix} -\sin\theta & 0 & \cos\theta \\ 0 & 0 & 0 \\ -\cos\theta & 0 & -\sin\theta \end{bmatrix}, \quad \dot{R}_{z}(\theta) = \dot{\theta} \begin{bmatrix} -\sin\theta & -\cos\theta & 0 \\ \cos\theta & -\sin\theta & 0 \\ 0 & 0 & 0 \end{bmatrix}. \quad (11)$$

## 3.2.2. ECEF to ECI

139

140

To convert from the ECEF to the ECI frame, we need to know the Greenwich Mean Sidereal Time,  $\Theta$ , at the moment the measurement was taken. We can compute  $\Theta$  from the UTC date and time, and we will assume that it is known exactly. The ECEF frame is rotating about the z axis at a rate  $\dot{\Theta} = 7.292115 \times 10^{-5}$  rad/s with respect to the ECI frame, so the conversion is written as

$$\mathbf{x}_{\text{ECI}} = \begin{bmatrix} R_z(\Theta) & 0\\ \dot{R}_z(\Theta) & R_z(\Theta) \end{bmatrix} \mathbf{x}_{\text{ECEF}}.$$
 (12)

#### 3.2.3. ECI to SCI

The final conversion from the ECI to SCI frame again requires us to know the time of the observation to determine the state of the Sun with respect to the Earth in the ECI frame  $x_{\rm ECI}^{\rm sun}$ , which we find using JPL DE430 ephemerides (Acton, 1996). Assuming this is known exactly, our conversion becomes

$$\mathbf{x}_{\text{SCI}} = \begin{bmatrix} R_x(-\epsilon) & 0\\ 0 & R_x(-\epsilon) \end{bmatrix} (\mathbf{x}_{\text{ECI}} - \mathbf{x}_{\text{ECI}}^{\text{sun}}),\tag{13}$$

where  $\varepsilon \approx 23.44^{\circ}$  is the angular offset of Earth's orbit from the ecliptic plane.

# 3.3. Dynamics and Perturbations

We propagate the state backward in time using the fundamental orbital differential equation in each frame

$$\ddot{r}_{\rm ECI} = -\frac{GM_{\oplus}}{r_{\rm ECI}^3} r_{\rm ECI} \tag{14}$$

$$\ddot{r}_{\text{SCI}} = -\frac{GM_{\odot}}{r_{\text{SCI}}^3} r_{\text{SCI}},\tag{15}$$

where  $G \approx 6.6 \times 10^{-20} \, \frac{\mathrm{km}^3}{\mathrm{s}^2 \mathrm{kg}}$  is the universal gravitational parameter,  $M_{\odot} \approx 1.989 \times 10^{30}$  kg is the mass of the Sun, and  $M_{\oplus} \approx 5.972 \times 10^{24}$  kg is the mass of the Earth. Note that we use the convention  $r_{\mathrm{SCI}} = \| \mathbf{r}_{\mathrm{SCI}} \|$ . We integrate from the initial observation back to one million km away from the Earth in the ECI frame to escape Earth's sphere of influence. Then we convert to SCI and integrate back to one billion kilometers from the Sun, which is farther than the orbit of Jupiter. If the orbit is asteroidal and never reaches that distance, the user can select a final integration time. We represent the evolution of the full state as a nonlinear ODE

$$\dot{\mathbf{x}}_{\text{SCI}} = \begin{bmatrix} 0 & I \\ -\frac{GM_{\odot}}{r_{\text{SCI}}^3} & 0 \end{bmatrix} \mathbf{x}_{\text{SCI}}.$$
 (16)

This is incomplete, as we need to include relevant orbital perturbations. We have included the option to add in perturbation effects from third-body forces, including the Moon and all the planets. We can also include atmospheric drag and solar radiation pressure if the mass and cross-sectional area of the meteoroid are known.

# 3.3.1. Third-Body Forces

157

158

159

162

163

The acceleration from third-body (TB) forces is

$$\ddot{\mathbf{r}}_{\mathrm{TB}} = \sum_{i} -\frac{GM_{i}}{r_{i}^{3}} \mathbf{r}_{i},\tag{17}$$

where  $M_i$  is the mass of body i, and  $r_i$  is the vector pointing from body i to the spacecraft. The integration is done first in the ECI frame, during which time the Sun and Moon cause the dominant TB perturbations. After converting to the SCI frame, the Earth and Jupiter cause the dominant TB perturbations. By propagating past the orbit of Jupiter, we can rule out any gravity assist effects it may have had on the meteoroid in question. The effects of the other planets are less important, but still available for the user to include.

# 3.3.2. Atmospheric Drag

The acceleration due to atmospheric drag is

$$\ddot{\mathbf{r}}_{\mathrm{D}} = -\frac{1}{2} C_{\mathrm{D}} \frac{A}{m} \rho v_{\mathrm{rel}} \mathbf{v}_{\mathrm{rel}} \tag{18}$$

where  $C_{\rm D}$  is the coefficient of drag, A and m are the cross-sectional area and mass of the particle, and  $v_{\rm rel}$  is the velocity vector of the particle relative to the atmosphere. We choose  $C_{\rm D}=0.5$  to approximate a sphere. The density of the atmosphere,  $\rho$ , is assumed to follow an exponential model

$$\rho = \rho_0 e^{-\frac{h}{H}},\tag{19}$$

where  $\rho_0$  is the density of the atmosphere at sea level, h is the altitude of the particle, and H is the scale height. We neglect the drag force once the meteoroid is above 180 km, therefore this perturbation is only included when integrating in the ECI frame. Vida et al. (2018) demonstrated that the initial velocity is negligibly affected by atmospheric density changes on the order of a factor of two, which justifies our use of the exponential density model.

#### 3.3.3. Solar Radiation Pressure

171

172

173

174

178

180

185

In most of the meteoroid orbit determination literature solar radiation pressure (SRP) is neglected. However, SRP becomes a significant perturbation for smaller particles like those detected by ALTAIR. SRP would work to lower the energy of any incoming interstellar particles, therefore it is an essential perturbation to consider when trying to identify interstellar meteoroids. The acceleration due to solar radiation pressure is

$$\ddot{\mathbf{r}}_{\text{SRP}} = \frac{G_{\text{sc}} \text{AU}^2}{cr_{\text{SCI}}^2} C_{\text{SRP}} \frac{A}{m} \hat{\mathbf{r}}_{\text{SCI}},\tag{20}$$

where  $G_{\rm sc}=1360.8~{\rm W/m^2}$  is the solar flux measured at one AU (1.496  $\times$  10<sup>11</sup> km) from the Sun,  $c=2.9979\times10^8$  m/s is the speed of light, and  $C_{\rm SRP}$  is the coefficient of absorption and reflection. We select  $C_{\rm SRP}=1$  to approximate pure absorption with no reflection.

#### 3.3.4. Full Perturbation

These accelerations are simply added to the right-hand side of the dynamics ODEs from Eqs. 14 and 15 as

$$\ddot{\mathbf{r}}_{\mathrm{ECI}} = -\frac{GM_{\odot}}{r_{\mathrm{ECI}}^{3}} \mathbf{r}_{\mathrm{ECI}} + \ddot{\mathbf{r}}_{\mathrm{D}} + \ddot{\mathbf{r}}_{\mathrm{SRP}} + \ddot{\mathbf{r}}_{\mathrm{TB}} \tag{21}$$

$$\ddot{r}_{\text{SCI}} = -\frac{GM_{\odot}}{r_{\text{SCI}}^3} r_{\text{SCI}} + \ddot{r}_{\text{SRP}} + \ddot{r}_{\text{TB}}.$$
(22)

We use a Runge-Kutta-Fehlberg 7-8 integration scheme with variable step size to integrate the equations of motion.

## 3.4. Computing Orbital Elements

After performing the integration in Cartesian coordinates, we compute the total mechanical energy

$$\mathcal{E} = \frac{1}{2}\dot{r}_{\text{SCI}}^2 - \frac{GM_{\odot}}{r_{\text{SCI}}}.$$
(23)

A positive mechanical energy is indicative of a hyperbolic orbit with respect to the sun and therefore an interstellar meteoroid. See Figure 6 for examples of elliptical and hyperbolic orbits. By characterizing the uncertainty around the mechanical energy, we can define a confidence bound on the region  $\mathcal{E} > 1$  and thereby define our confidence in the interstellar classification.

Finally, we compute the orbital elements

$$a = -\frac{GM_{\odot}}{2\mathcal{E}} \tag{24}$$

$$e = \frac{1}{GM_{\odot}} ((\dot{\mathbf{r}}_{\text{SCI}}^T \dot{\mathbf{r}}_{\text{SCI}} - \frac{GM_{\odot}}{r_{\text{SCI}}}) \mathbf{r} - (\mathbf{r}_{\text{SCI}}^T \dot{\mathbf{r}}_{\text{SCI}}) \dot{\mathbf{r}}_{\text{SCI}})$$
(25)

$$e = ||e|| \tag{26}$$

$$h = r_{\text{SCI}} \times \dot{r}_{\text{SCI}} \tag{27}$$

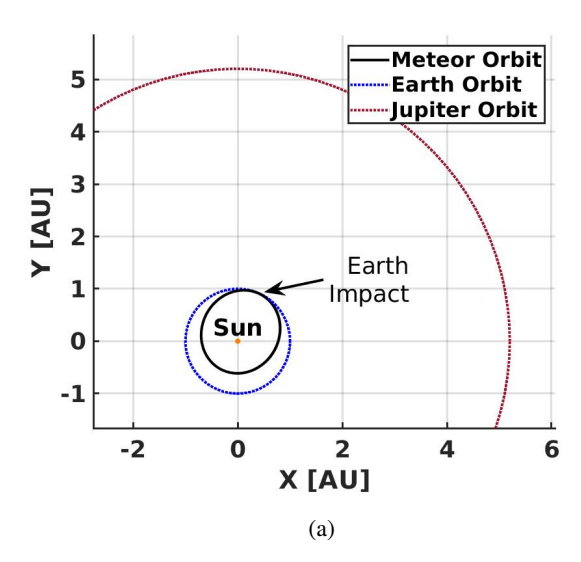
$$i = \arccos\frac{h_z}{h} \tag{28}$$

$$\mathbf{n} = \begin{bmatrix} 0 & 0 & 1 \end{bmatrix}^T \times \mathbf{h} \tag{29}$$

$$\Omega = \arccos \frac{n_x}{n} \tag{30}$$

$$\omega = \arccos \hat{e}^T \hat{r}_{SCI},\tag{31}$$

where a is the semi-major axis, e is the eccentricity, i is the inclination,  $\Omega$  is the right ascension of the ascending node, and  $\omega$  is the argument of periapsis. The eccentricity vector e, angular momentum vector e, and tilt vector e, are intermediate objects used to compute the orbital elements.



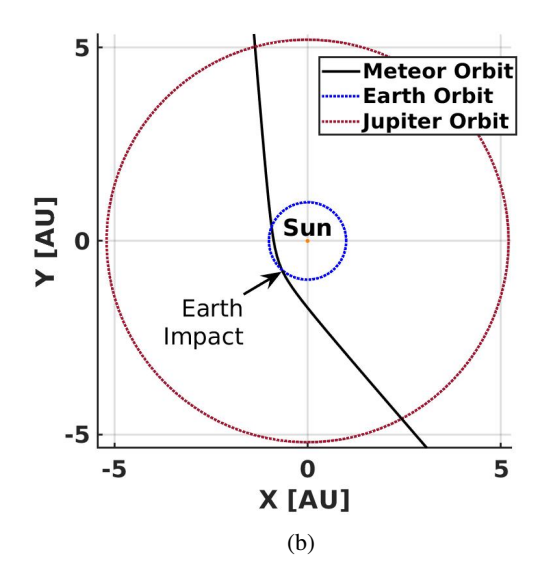


Figure 6: Some meteoroids come from asteroids or other bodies in the inner solar system and impact Earth from elliptical orbits as shown in 6a. Others impact Earth from hyperbolic orbits as shown in 6b. This means that they must have originated from outside the solar system unless they received a gravity assist from another planet.

# 4. Uncertainty Propagation

Following the work of Dmitriev et al. (2015), we use strict covariance transformations to estimate the uncertainties in the orbital elements given the initial dispersions. We have compared this method against a "ground truth" Monte Carlo model that samples 1000 measurements from the initial distribution and computes the distributions of the orbital elements after backward propagation.

#### 4.1. Prior

189

190

191

192

193

195

196

197

The ALTAIR data set contains prior information in spherical coordinates in ENU frame. We assume that the time, radar location, and radar pointing direction are all known exactly. However, we have standard deviations in the other quantities, so our initial covariance matrix can be written as

$$\Sigma_0 = \operatorname{diag}(\sigma_r^2, \, \sigma_\alpha^2, \, \sigma_\beta^2, \, \sigma_{\dot{r}}^2, \, \sigma_{\dot{\alpha}}^2, \, \sigma_{\dot{\beta}}^2). \tag{32}$$

# 4.2. Covariance Transforms

## 4.2.1. spherical to cartesian analytical expression

While the conversion from  $x_{sph}$  to  $x_{ENU}$  is nonlinear, we can still transform our covariance matrix analytically by using the Jacobian,  $J_1$ , of the transform  $f_1$  from Eq. 4

$$\Sigma_1 = J_1 \Sigma_0 J_1^T \tag{33}$$

$$J_1 = \frac{\partial f_1}{\partial \mathbf{x}_{\text{sph}}}.$$
 (34)

The Jacobians of various nonlinear transformation used in the frame conversions are

$$J_1 = \begin{bmatrix} J_{11} & 0 \\ J_{21} & J_{22} \end{bmatrix} \tag{35}$$

$$J_{1} = \begin{bmatrix} J_{11} & 0 \\ J_{21} & J_{22} \end{bmatrix}$$

$$J_{11} = J_{22} = \begin{bmatrix} c_{\beta}s_{\alpha} & rc_{\beta}c_{\alpha} & -rs_{\beta}s_{\alpha} \\ c_{\beta}c_{\alpha} & -rc_{\beta}s_{\alpha} & -rs_{\beta}c_{\alpha} \\ s_{\beta} & 0 & rc_{\beta} \end{bmatrix}$$

$$(35)$$

$$J_{21} = \begin{bmatrix} \dot{\alpha}c_{\beta}c_{\alpha} - \dot{\beta}s_{\beta}s_{\alpha} & \dot{r}c_{\beta}c_{\alpha} - r\dot{\alpha}c_{\beta}s_{\alpha} - r\dot{\beta}s_{\beta}c_{\alpha} & -\dot{r}s_{\beta}s_{\alpha} - r\dot{\alpha}s_{\beta}c_{\alpha} - r\dot{\beta}c_{\beta}s_{\alpha} \\ -\dot{\alpha}c_{\beta}s_{\alpha} - \dot{\beta}s_{\beta}c_{\alpha} & \dot{r}c_{\beta}s_{\alpha} - r\dot{\alpha}c_{\beta}c_{\alpha} + r\dot{\beta}s_{\beta}s_{\alpha} & -\dot{r}s_{\beta}c_{\alpha} + r\dot{\alpha}s_{\beta}s_{\alpha} - r\dot{\beta}c_{\beta}c_{\alpha} \\ \dot{\beta}c_{\beta} & 0 & \dot{r}c_{\beta} - r\dot{\beta}s_{\beta} \end{bmatrix},$$

$$(37)$$

where  $s_{\alpha} = \sin \alpha$  and  $c_{\beta} = \cos \beta$ . We next convert to the ECI frame. Since we assume to know the time, radar location, and position of the sun exactly, the conversion leaves us with

$$\Sigma_2 = R_2 \Sigma_1 R_2^T \tag{38}$$

$$R_2 = \begin{bmatrix} R_z(\Theta) & 0 \\ \dot{R}_z(\Theta) & R_z(\Theta) \end{bmatrix} \begin{bmatrix} R_z(\pi/2 + \lambda)R_x(\pi/2 - \phi) & 0 \\ 0 & R_z(\pi/2 + \lambda)R_x(\pi/2 - \phi) \end{bmatrix}. \tag{39}$$

We propagate our state through time according to the dynamics ODE in Eq. 21 and compute the state transition matrix  $\Phi(t,0)$  by propagating it along with the state according to the ODE

$$\dot{\Phi} = \begin{bmatrix} 0 & I \\ \frac{\partial \ddot{r}_{\text{ECI}}}{\partial r_{\text{ECI}}} & \frac{\partial \ddot{r}_{\text{ECI}}}{\partial \dot{r}_{\text{ECI}}} \end{bmatrix} \Phi. \tag{40}$$

Note that  $\frac{\partial \vec{r}_{ECI}}{\partial r_{ECI}}$  and  $\frac{\partial \vec{r}_{ECI}}{\partial \vec{r}_{ECI}}$  change depending on which perturbations are included (Montenbruck and Gill, 2012, Sec. 7.3). For the pure two-body case with no perturbations we write

$$\frac{\partial \ddot{\mathbf{r}}_{\text{ECI}}}{\partial \dot{\mathbf{r}}_{\text{ECI}}} = 0 \tag{41}$$

$$\frac{\partial \ddot{\mathbf{r}}_{\text{ECI}}}{\partial \mathbf{r}_{\text{ECI}}} = \frac{GM_{\odot}}{r_{\text{ECI}}^{5}} \begin{bmatrix} 3x_{\text{ECI}}^{2} - r_{\text{ECI}}^{2} & 3x_{\text{ECI}}y_{\text{ECI}} & 3x_{\text{ECI}}z_{\text{ECI}} \\ 3y_{\text{ECI}}x_{\text{ECI}} & 3y_{\text{ECI}}^{2} - r_{\text{ECI}}^{2} & 3y_{\text{ECI}}z_{\text{ECI}} \\ 3z_{\text{ECI}}x_{\text{ECI}} & 3z_{\text{ECI}}y_{\text{ECI}} & 3z_{\text{ECI}}^{2} - r_{\text{ECI}}^{2} \end{bmatrix}.$$
(42)

When including perturbations,  $\frac{\partial \ddot{r}_{ECI}}{\partial r_{ECI}}$  and  $\frac{\partial \ddot{r}_{ECI}}{\partial \dot{r}_{ECI}}$  gain additional terms. The partial derivatives associated with drag are

$$\frac{\partial \ddot{\mathbf{r}}_{\text{drag}}}{\partial \dot{\mathbf{r}}_{\text{ECI}}} = -\frac{1}{2} C_{\text{D}} \frac{A}{m} \rho \left( \frac{v_{\text{rel}} v_{\text{rel}}^T}{v_{\text{rel}}} + v_{\text{rel}} I \right)$$
(43)

$$\frac{\partial \ddot{\mathbf{r}}_{\text{drag}}}{\partial \mathbf{r}_{\text{ECI}}} = -\frac{1}{2} C_{\text{D}} \frac{A}{m} v_{\text{re}} v_{\text{rel}} \frac{-\rho_0}{H} e^{\frac{-h}{H}} - \frac{\partial \ddot{\mathbf{r}}_{\text{drag}}}{\partial \dot{\mathbf{r}}_{\text{ECI}}} \begin{bmatrix} 0 & -\dot{\Theta} & 0\\ \dot{\Theta} & 0 & 0\\ 0 & 0 & 0 \end{bmatrix}. \tag{44}$$

206 The partial derivatives associated with SRP are

$$\frac{\partial \ddot{\mathbf{r}}_{SRP}}{\partial \dot{\mathbf{r}}_{SCI}} = 0 \tag{45}$$

$$\frac{\partial \ddot{\mathbf{r}}_{\text{SRP}}}{\partial \mathbf{r}_{\text{SCI}}} = \frac{G_{\text{sc}} \text{AU}^2}{c} C_{\text{SRP}} \frac{A}{m} \left( \frac{1}{r_{\text{SCI}}^3} I - \frac{3}{r_{\text{SCI}}^5} r_i r_i^T \right). \tag{46}$$

207 The partial derivatives associated with third-body forces are

$$\frac{\partial \ddot{\mathbf{r}}_{\mathrm{TB}}}{\partial \dot{\mathbf{r}}} = 0 \tag{47}$$

$$\frac{\partial \ddot{\mathbf{r}}_{\text{TB}}}{\partial \mathbf{r}} = \sum_{i} -GM_{i} \left( \frac{1}{r_{i}^{3}} I - \frac{3}{r_{i}^{5}} r_{i} r_{i}^{T} \right), \tag{48}$$

where  $r_i$  is the vector from body i to the spacecraft in the frame of integration. Once we have computed the state transition matrix in the ECI frame, we can use it to update the covariance matrix from  $\Sigma_2$  to  $\Sigma_3$ 

$$\Sigma_3 = \Phi(t, 0)_{\text{ECI}} \Sigma_2 \Phi(t, 0)_{\text{ECI}}^T. \tag{49}$$

Then we convert to SCI and update the covariance matrix as

$$\Sigma_4 = R_4 \Sigma_3 R_4^T \tag{50}$$

$$R_4 = \begin{bmatrix} R_{\chi}(-\epsilon) & 0 \\ 0 & R_{\chi}(-\epsilon) \end{bmatrix}. \tag{51}$$

We integrate in the SCI frame using equation 22. We compute the state transition matrix using Eq. 40, replacing  $r_{\rm ECI}$  with  $r_{\rm SCI}$ , and use the computed state transition matrix to update the covariance matrix again

$$\Sigma_5 = \Phi(t, 0)_{\text{SCI}} \Sigma_4 \Phi(t, 0)_{\text{SCI}}^T. \tag{52}$$

We then compute the mechanical energy of the meteor as shown in Eq. 23. We use the partial derivative of the mechanical energy with respect to the final state to compute the variance of  $\mathcal{E}$ 

$$\sigma_{\mathcal{E}}^2 = J_{\mathcal{E}} \Sigma_5 J_{\mathcal{E}}^T \tag{53}$$

$$J_{\mathcal{E}} = \frac{\partial \mathcal{E}}{\partial \mathbf{x}_{\text{SCI}}} = \begin{bmatrix} \frac{GM_{\odot}}{r_{\text{SCI}}^3} \mathbf{r}_{\text{SCI}}^T & \dot{\mathbf{r}}_{\text{SCI}}^T \end{bmatrix}. \tag{54}$$

We can compute the variances of each of the orbital elements using the matrix of partial derivatives of the orbital elements with respect to the cartesian state vector as described by Montenbruck and Gill (2012)

$$\begin{bmatrix} \sigma_a^2, & \sigma_e^2, & \sigma_i^2, & \sigma_\omega^2 \end{bmatrix}^T = J_{\text{o.e.}} \Sigma_5 J_{\text{o.e.}}$$
(55)

$$J_{\text{o.e.}} = \frac{\partial(a, e, i, \Omega, \omega)}{\partial \mathbf{x}_{\text{SCI}}}.$$
 (56)

# 4.3. Computational Speed

When we use this covariance transform method, we can integrate the state transition matrix simultaneously with the meteoroid orbit, which saves computational time. The Monte Carlo method doesn't require as much computation per sample, but requires many samples to provide an accurate estimate of the orbital element dispersions. We found that the covariance transform method is about 30x faster than Monte Carlo with 1000 samples when neglecting perturbations. Adding in perturbations slows down the Monte Carlo method even more and the covariance transform method runs about 100x faster.

#### 5. Results

220

221

222

223

226

230

231

233

235

236

We verified our computations by comparing them with the orbits of several fireballs registered by the Finnish Fireball Network computed by Dmitriev et al. (2015) as well as the orbit of the Hayabusa spacecraft as described by Jansen-Sturgeon et al. (2019). To compare orbits we use the similarity index created by Southworth and Hawkins (1963)

$$\begin{split} D(A,B)^2 &= \left(e_B - e_A\right)^2 + \left(q_B - q_A\right)^2 + \left(2\sin\frac{i_B - i_A}{2}\right)^2 \\ &+ \sin i_A \sin i_B \left(2\sin\frac{\Omega_B - \Omega_A}{2}\right)^2 + \left(\left(\frac{e_A + e_B}{2}\right)2\sin\frac{(\Omega_B + \omega_B) - (\Omega_A + \omega_A)}{2}\right)^2. \end{split}$$

A similarity index of D = 0 corresponds to identical orbits A and B. Similarity index values of 0 < D < 1e-5 are considered negligible and can be caused by numerical error or small differences in constant values used, like the radius or the angular rotation rate of the Earth. We saw good agreement between our results and those produced using the Meteor Toolkit, as shown in Table 3. The standard deviations produced by MODA also showed good agreement with those produced by the Meteor Toolkit as shown in Table 4.

All the results from Dmitriev et al. (2015) in Table 3 except Kosice were computed without drag or SRP effects as the mass and cross-sectional area of meteoroids were not known. The Kosice fireball was originally described by Borovička et al. (2013) and included in Dmitriev's analysis due to its well known mass and bulk density. The orbits for the Kosice meteor and the Hayabusa spacecraft were computed with drag and SRP effects included. Drag is shown to have a small effect, and the effect from SRP is almost non-existent.

**Table 2** Measured topocentric radiants of meteors used for verification. The symbols  $\phi_t$ ,  $\lambda_t$ , and  $h_t$  correspond to the geodetic latitude, longitude, and altitude of the initial point of the fireball, while  $\alpha_t$ ,  $\beta_t$ , and  $v_t$  correspond to the apparent azimuth, elevation, and velocity. The standard deviations are found beneath each value, except for the Hayabusa Spacecraft, which didn't have standard deviation values available.

Name	Date	$\phi_t$ [deg]	$\lambda_t$ [deg]	$h_t$ [km]	$\alpha_t$ [deg]	$\beta_t$ [deg]	$v_t$ [km/s]	$A [m^2]$	<i>m</i> [kg]
Oijarvi	2010/12/26	64.78	26.91	77.00	156.20	25.80	13.80	-	-
Oljarvi	14:06:09.0	$\pm 0.02$	$\pm 0.01$	$\pm 1.00$	±0.30	$\pm 0.30$	$\pm 1.00$	-	-
Mikkeli	2013/09/13	61.46	26.90	82.10	238.94	55.06	14.98	-	-
IVIIKKEII	22:33:37.0	±0.01	±0.01	$\pm 0.50$	±0.40	$\pm 0.20$	±0.10	-	-
Annama	2014/04/18	67.93	30.76	83.90	176.10	34.32	24.21	-	-
Alliallia	22:14:09.3	±0.01	±0.01	$\pm 0.50$	±0.50	$\pm 0.50$	±0.50	-	-
Haapavesi	2014/09/25	66.52	25.16	70.95	357.25	11.05	14.78	-	-
Haapavesi	03:12:15.0	±0.03	±0.02	$\pm 1.00$	±0.30	$\pm 0.30$	±0.30	-	-
Kosice	2010/02/28	48.667	20.705	68.3	252.6	59.8	15.0	1.23	3500
Nosice	22:24:47.0	$\pm 0.021$	$\pm 0.011$	±1.4	<u>+</u> 4.0	$\pm 2.0$	±0.3		
Hayabusa	2010/06/13	-29.0243	131.1056	99.880	290.5220	10.0173	11.7251	2.15	415
Spacecraft	13:51:56.6								

Table 3 Comparison of orbit computations made using the Meteor Toolkit and MODA. The similarity index D between our results and those of the Meteor Toolkit show that any differences are likely numerical in nature or have to do with slight differences in certain constants (e.g. radius of the Earth). When adding in third-body (TB) perturbations, the similarity index increases by about two orders of magnitude.

Name	Method	a [AU]	e	i [deg]	$\Omega$ [deg]	$\omega$ [deg]	D
	Meteor Toolkit	2.46	0.601	2.80	94.5	353	-
Oijarvi	MODA (no pert)	2.47	0.603	2.81	94.5	353	2.71e-06
	MODA (TB)	2.47	0.604	2.80	94.6	350	8.90e-04
	Meteor Toolkit	1.44	0.365	12.2	171	230	-
Mikkeli	MODA (no pert)	1.44	0.366	12.2	171	230	1.71e-06
	MODA (TB)	1.42	0.348	12.2	171	227	6.08e-04
	Meteor Toolkit	2.00	0.683	14.6	28.6	265	-
Annama	MODA (no pert)	2.00	0.683	14.6	28.6	265	1.24e-07
	MODA (TB)	1.95	0.672	14.6	28.7	264	1.31e-04
	Meteor Toolkit	2.53	0.604	9.24	182	175	-
Haapavesi	MODA (no pert)	2.54	0.606	9.25	182	175	3.93e-06
	MODA (TB)	2.54	0.606	9.22	182	172	6.24e-04
	Meteor Toolkit	2.73	0.649	2.02	340	204	-
Kosice	MODA (no pert)	2.76	0.654	1.95	340	204	3.28e-05
	MODA (TB)	2.68	0.640	1.94	340	202	7.85e-04
	$MODA\ (TB + drag)$	2.70	0.642	1.95	340	202	7.31e-04
	MODA (TB + drag + SRP)	2.70	0.642	1.95	340	202	7.31e-04
Havabusa	Telemetry	1.32	0.257	1.68	82.5	147	-
Hayabusa	MODA (no pert)	1.33	0.259	1.70	82.4	148	4.26e-06
	MODA (TB)	1.34	0.279	1.69	82.5	141	1.65e-03
	MODA (TB + drag)	1.34	0.279	1.69	82.5	141	1.65e-03
	MODA (TB + drag + SRP)	1.34	0.279	1.69	82.5	141	1.65e-03

Once we had verified our computations against previously computed orbits, we used MODA to compute the orbits of two meteors observed by ALTAIR in 2008, shown in Figures 7 and 8. These are the same meteors that produced the measurements shown earlier in Figure 4. Tables 5 and 6 show the measured topocentric states and computed orbital elements for these two meteors. They were observed 12 minutes apart at 113 km altitude, but ALTAIR-4 had a range rate about 13% greater than that of ALTAIR-3. Both appear to originate from highly inclined orbits. As expected

238 239 240

**Table 4**Comparison of the standard deviations of the orbital elements computed using the Meteor Toolkit and this method show good agreement, at least to an order of magnitude in most cases.

Name	Method	$\sigma_a$ [AU]	$\sigma_e$	$\sigma_i$ [deg]	$\sigma_{\Omega}$ [deg]	$\sigma_{\omega}$ [deg]
Oijarvi	Meteor Toolkit	0.512	0.0830	0.218	2.00e-04	0.276
Oljarvi	MODA (no pert)	0.924	0.149	0.457	0.0134	0.433
Mikkeli	Meteor Toolkit	0.0114	5.30e-03	0.132	4.00e-04	0.304
Mikkeli	MODA (no pert)	0.0111	5.30e-03	0.193	7.00e-04	0.410
Annama	Meteor Toolkit	0.107	0.0180	0.504	5.00e-04	1.10
Allilalila	MODA (no pert)	0.121	0.0204	0.562	7.00e-04	1.05
Haanayasi	Meteor Toolkit	0.111	0.0173	0.351	1.70e-03	0.313
Haapavesi	MODA (no pert)	0.161	0.0250	0.607	3.70e-03	0.226
Kosice	Meteor Toolkit	0.225	0.0290	0.903	0.0310	1.58
	MODA (no pert)	0.289	0.0346	0.661	0.0238	1.80

 Table 5

 Measured topocentric states in ENU frame for ALTAIR meteors with standard deviations beneath.

Name	Time	<i>r</i> [km]	$\alpha$ [deg]	β [deg]	<i>r</i> [km/s]	$\dot{\alpha}  [\text{deg/s}]$	$\dot{\beta}$ [deg/s]	A/m [m <sup>2</sup> /kg]
ALTAIR-3	January 02, 2008	113.079	77.1	73.9	-53.9	-23.7	-11.2	4
ALIAIK-3	18:10:25.316	0.012	0.6	0.15	0.3	4.8	1.0	-
ALTAIR-4	January 02, 2008	113.661	76.6	73.9	-60.4	-14.2	8.2	4
ALIAIR-4	18:22:35.529	0.010	0.3	0.18	0.16	1.7	0.7	-

**Table 6**Orbital elements for ALTAIR meteors computed by MODA with various perturbations. We also computed the standard deviations of the orbital elements for the case with all three perturbations. Both the Monte Carlo and covariance transform methods yielded approximately the same standard deviation values.

Name	Perturbations	a [AU]	e	i [deg]	$\Omega$ [deg]	$\omega$ [deg]
	None	1.0	0.39	169.9	101.6	114.9
	ТВ	1.0	0.39	169.9	101.6	115.1
ALTAIR-3	TB + drag	1.1	0.39	170.3	101.6	96.2
	TB + drag + SRP	1.1	0.39	170.3	101.6	95.6
		$\pm 0.14$	$\pm 0.076$	$\pm 4.4$	± 0.2	$\pm 11.8$
	None	2.6	0.74	136.7	281.6	104.4
	ТВ	2.6	0.75	136.7	281.6	104.3
ALTAIR-4	TB + drag	5.1	0.86	137.9	281.6	112.8
	TB + drag + SRP	5.3	0.87	137.9	281.6	113.1
		± 2.2	$\pm 0.059$	$\pm 1.8$	$\pm 0.0087$	$\pm 1.9$

from the lower range-rate, ALTAIR-3 has a smaller semi-major axis (a = 1.1 AU). Note that the semi-major axis of ALTAIR-4 (a = 5.3 AU)) is highly dependent on the inclusion of drag forces in the integration, much more so than ALTAIR-4. For both meteoroids, atmospheric drag is the most important perturbation to include. The oversized effect of drag is attributed to the estimated area to mass ratio for these particles, which at A/m = 4 m<sup>2</sup>/kg is several orders of magnitude larger than those of Kosice (A/m = 3.5e-04 m<sup>2</sup>/kg) and the Hayabusa spacecraft (A/m = 0.0052 m<sup>2</sup>/kg). The standard deviations of the orbital elements for the perturbed cases are generally small. The exceptions are argument of periapsis ( $\omega$ ) for ALTAIR-3 and semimajor axis (a) for ALTAIR-4.

# 6. Discussion

243

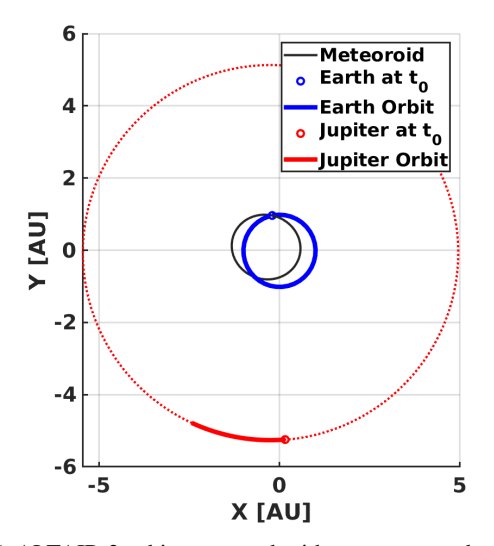
244

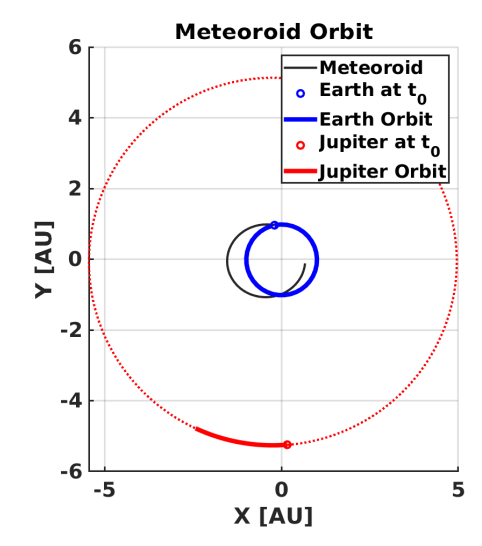
245

246

251

There is a general agreement of the MODA results with those of the Meteor Toolkit and the uncertainties computed for the ALTAIR micrometeoroids are of roughly the same order of magnitude as those of the larger meteoroids. What's more, the standard deviations produced by the covariance transform method match those produced by the Monte Carlo

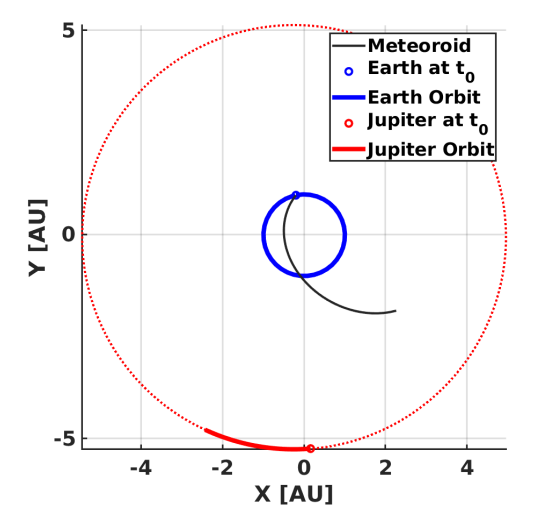


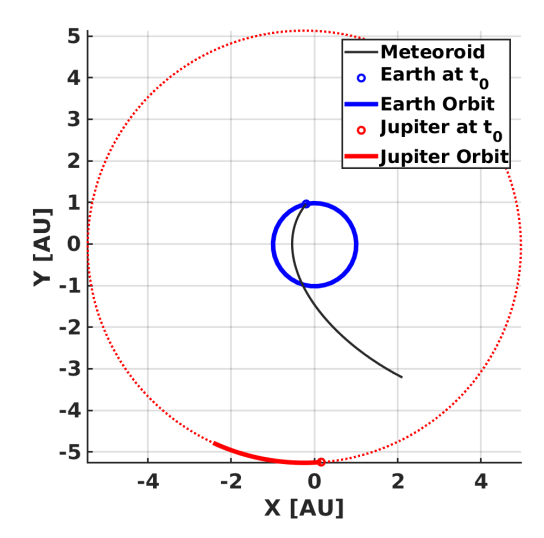


(a) ALTAIR-3 orbit computed without any perturbations. The Sun-centric semi-major axis and eccentricity are a = 1.0 AU and e = 0.39. The orbit has been propagated backwards for one year.

(b) ALTAIR-3 orbit computed with drag, SRP, and third-body effects from the Moon and Jupiter. The Sun-centric semi-major axis and eccentricity are a = 1.1 AU and e = 0.39.

Figure 7: ALTAIR-3 orbit propagated backward in time from observation.





(a) ALTAIR-4 orbit computed without any perturbations. The Sun-centric semi-major axis and eccentricity are a = 2.6 AU and e = 0.74. The orbit has been propagated backwards for one year.

(b) ALTAIR-4 orbit computed with drag, SRP, and third-body effects from the Moon and Jupiter. The Sun-centric semi-major axis and eccentricity are a = 5.3 AU and e = 0.87.

Figure 8: ALTAIR-4 orbit propagated backward in time from observation.

method. This leads us to believe that MODA is a reasonably accurate tool that will be useful for HPLA radar data.

Atmospheric drag and SRP had a much larger effect on the orbital elements of the ALTAIR meteoroids than on Kosice and the Hayabusa spacecraft, for which SRP effects were essentially non-existent. This is expected, as the area to mass ratios of the ALTAIR meteoroids are orders of magnitude greater than those of Kosice and Hayabusa.

Since atmospheric drag and SRP forces are proportional to the surface area to mass ratio, we are likely neglecting a significant source of uncertainty by assuming that A/m is known exactly.

# 7. Conclusion

259

261

263

265

266

270

271

272

We have developed MODA, an open-source tool in MATLAB for computing meteoroid orbits. While our code works for any type of meteoroid, it is designed with the small particles observable by HPLA radar in mind. We use a numerical integration scheme, which has been shown to outperform the analytical approximations used frequently in the literature. It also allows us to take drag, SRP, and third-body effects into account. We included SRP due to its significance to very small particles. MODA computes the uncertainty of the orbital elements by using the covariance transform method, which runs many times faster than Monte Carlo simulations.

We applied MODA to two meteoroids observed by the ALTAIR HPLA radar facility in 2008. Our results demonstrated that the orbital element uncertainties for micrometeoroids observed with ALTAIR have roughly the same order of magnitude as those for larger meteoroids. They also affirm that atmospheric drag and SRP effects are much more pronounced on the small particles observed by HPLA radars.

Future work will include adding in prior probability distributions for the area to mass ratio of the meteor, atmospheric density, and coefficient of drag. Also, we would like to determine whether other effects such as Lorentz forces, Poynting-Robertson drag, and the Yarkovsky effect may have significant effects on the orbital elements of micrometeoroids.

# 8. Acknowledgment

This work was funded by the National Science Foundation under Grant AGS-1920383. The software produced by this work makes use of Mice, the freely available ANSI C based interface between the MATLAB environment and the CSPICE library, developed by Ed Wright at the Jet Propulsion Laboratory.

#### References

- Acton, C.H., 1996. Ancillary data services of NASA's navigation and Ancillary Information Facility. Planetary and Space Science 44, 65–70. doi:10.1016/0032-0633(95)00107-7.
- 278 Andersson, J., 2018. Determination of the Orbit and Dynamic Origin of Meteoroids. Ph.D. thesis. Uppsala Universitet.
- Baggaley, W.J., Marsh, S.H., Close, S., 2007. Interstellar meteors. Dust in Planetary Systems ESA SP-643.
- Borovička, J., Spurný, P., Brown, P.G., Wiegert, P., Kalenda, P., Clark, D.L., Shrbený, L., 2013. The trajectory, structure and origin of the Chelyabinsk asteroidal impactor. Nature 503, 235–237. URL: http://arxiv.org/abs/1306.1622, doi:10.1038/nature12671.
- Brown, P.G., Hunt, S.M., Close, S., 2001. Astronomical and physical data for meteoroids recorded by the ALTAIR radar. Technical Report. Los
  Alamos National Laboratory. URL: https://www.osti.gov/biblio/975805.
- Campbell-Brown, M.D., Close, S., 2007. Meteoroid structure from radar head echoes. Monthly Notices of the Royal Astronomical Society 382, 1309–1316. URL: https://academic.oup.com/mnras/article/382/3/1309/1010752?login=true, doi:10.1111/j.1365-2966. 2007.12471.x.
- Ceplecha, Z., 1987. Geometric, dynamic, orbital and photometric data on meteoroids from photographic fireball networks. Bulletin of the Astronomical Institutes of Czechoslovakia 38, 222–234.
- Christou, A., Atreya, P., 2006. The Armagh Observatory meteor camera system. International Meteor Conference 1, 141–145.
- Clark, D.L., Wiegert, P.A., 2011. A numerical comparison with the Ceplecha analytical meteoroid orbit determination method. Meteoritics and
   Planetary Science 46, 1217–1225. doi:10.1111/j.1945-5100.2011.01226.x.
- Close, S., Hunt, S.M., McKeen, F.M., Minardi, M.J., 2002. Characterization of Leonid meteor head echo data collected using the VHFUHF Advanced Research Projects Agency Long-Range Tracking and Instrumentation Radar (ALTAIR). Radio Science 37, 9-1.
  URL: https://agupubs.onlinelibrary.wiley.com/doi/full/10.1029/2000RS002602https://agupubs.onlinelibrary.wiley.com/doi/10.1029/2000RS002602,
  doi:10.1029/2000rs002602.
- Close, S., Kelley, M., Vertatschitsch, L., Colestock, P., Oppenheim, M., Yee, J., 2011. Polarization and scattering of a long-duration meteor trail. Journal of Geophysical Research: Space Physics 116, 1309. URL: https://agupubs.onlinelibrary.wiley.com/doi/full/10.1029/2010JA015968https://agupubs.onlinelibrary.wiley.com/doi/abs/10.1029/2010JA015968https://agupubs.onlinelibrary.wiley.com/doi/10.1029/2010JA015968.
- Close, S., Volz, R., Loveland, R., Macdonell, A., Colestock, P., Linscott, I., Oppenheim, M., 2012. Determining meteoroid bulk densities using a plasma scattering model with high-power large-aperture radar data. Icarus 221, 300–309. doi:10.1016/j.icarus.2012.07.033.
- Colas, F., Zanda, B., Bouley, S., Jeanne, S., Malgoyre, A., Birlan, M., Blanpain, C., Gattacceca, J., Jorda, L., Lecubin, J., Marmo, C., Rault,
   J.L., Vaubaillon, J., Vernazza, P., Yohia, C., Gardiol, D., Nedelcu, A., Poppe, B., Rowe, J., Forcier, M., Koschny, D., Trigo-Rodriguez, J.M.,
   Lamy, H., Behrend, R., Ferrière, L., Barghini, D., Buzzoni, A., Carbognani, A., Di Carlo, M., Di Martino, M., Knapic, C., Londero, E., Pratesi,
   G., Rasetti, S., Riva, W., Stirpe, G.M., Valsecchi, G.B., Volpicelli, C.A., Zorba, S., Coward, D., Drolshagen, E., Drolshagen, G., Hernandez,

```
O., Jehin, E., Jobin, M., King, A., Nitschelm, C., Ott, T., Sanchez-Lavega, A., Toni, A., Abraham, P., Affaticati, F., Albani, M., Andreis, A.,
307
         Andrieu, T., Anghel, S., Antaluca, E., Antier, K., Appéré, T., Armand, A., Ascione, G., Audureau, Y., Auxepaules, G., Avoscan, T., Baba Aissa,
308
         D., Bacci, P., Bădescu, O., Baldini, R., Baldo, R., Balestrero, A., Baratoux, D., Barbotin, E., Bardy, M., Basso, S., Bautista, O., Bayle, L.D.,
309
         Beck, P., Bellitto, R., Belluso, R., Benna, C., Benammi, M., Beneteau, E., Benkhaldoun, Z., Bergamini, P., Bernardi, F., Bertaina, M.E., Bessin,
310
         P., Betti, L., Bettonvil, F., Bihel, D., Birnbaum, C., Blagoi, O., Blouri, E., Boacă, I., Boată, R., Bobiet, B., Bonino, R., Boros, K., Bouchet,
311
         E., Borgeot, V., Bouchez, E., Boust, D., Boudon, V., Bouman, T., Bourget, P., Brandenburg, S., Bramond, P., Braun, E., Bussi, A., Cacault,
312
         P., Caillier, B., Calegaro, A., Camargo, J., Caminade, S., Campana, A.P., Campbell-Burns, P., Canal-Domingo, R., Carell, O., Carreau, S.,
313
         Cascone, E., Cattaneo, C., Cauhape, P., Cavier, P., Celestin, S., Cellino, A., Champenois, M., Chennaoui Aoudjehane, H., Chevrier, S., Cholvy,
314
         P., Chomier, L., Christou, A., Cricchio, D., Coadou, P., Cocaign, J.Y., Cochard, F., Cointin, S., Colombi, E., Colque Saavedra, J.P., Corp, L.,
315
         Costa, M., Costard, F., Cottier, M., Cournoyer, P., Coustal, E., Cremonese, G., Cristea, O., Cuzon, J.C., D'agostino, G., Daiffallah, K., Dănescu,
316
         C., Dardon, A., Dasse, T., Davadan, C., Debs, V., Defaix, J.P., Deleflie, F., D'elia, M., De Luca, P., De Maria, P., Deverchère, P., Devillepoix,
317
         H., Dias, A., Di Dato, A., Di Luca, R., Dominici, F.M., Drouard, A., Dumont, J.L., Dupouv, P., Duvignac, L., Egal, A., Erasmus, N., Esseiva,
318
         N., Ebel, A., Eisengarten, B., Federici, F., Feral, S., Ferrant, G., Ferreol, E., Finitzer, P., Foucault, A., Francois, P., Frâncu, M., Froger, J.L.,
319
         Gaborit, F., Gagliarducci, V., Galard, J., Gardavot, A., Garmier, M., Garnung, M., Gautier, B., Gendre, B., Gerard, D., Gerardi, A., Godet,
320
         J.P., Grandchamps, A., Grouiez, B., Groult, S., Guidetti, D., Giuli, G., Hello, Y., Henry, X., Herbreteau, G., Herpin, M., Hewins, P., Hillairet,
321
         J.J., Horak, J., Hueso, R., Huet, E., Huet, S., Hyaumé, F., Interrante, G., Isselin, Y., Jeangeorges, Y., Janeux, P., Jeanneret, P., Jobse, K., Jouin,
322
         S., Jouvard, J.M., Joy, K., Julien, J.F., Kacerek, R., Kaire, M., Kempf, M., Koschny, D., Krier, C., Kwon, M.K., Lacassagne, L., Lachat, D.,
323
         Lagain, A., Laisné, E., Lanchares, V., Laskar, J., Lazzarin, M., Leblanc, M., Lebreton, J.P., Lecomte, J., Le Dû, P., Lelong, F., Lera, S., Leoni,
324
         J.F., Le-Pichon, A., Le-Poupon, P., Leroy, A., Leto, G., Levansuu, A., Lewin, E., Lienard, A., Licchelli, D., Locatelli, H., Loehle, S., Loizeau,
325
         D., Luciani, L., Maignan, M., Manca, F., Mancuso, S., Mandon, E., Mangold, N., Mannucci, F., Maquet, L., Marant, D., Marchal, Y., Marin,
326
         J.L., Martin-Brisset, J.C., Martin, D., Mathieu, D., Maury, A., Mespoulet, N., Meyer, F., Meyer, J.Y., Meza, E., Moggi Cecchi, V., Moiroud,
         J.J., Millan, M., Montesarchio, M., Misiano, A., Molinari, E., Molau, S., Monari, J., Monflier, B., Monkos, A., Montemaggi, M., Monti, G.,
328
         Moreau, R., Morin, J., Mourgues, R., Mousis, O., Nablanc, C., Nastasi, A., Niacşu, L., Notez, P., Ory, M., Pace, E., Paganelli, M.A., Pagola,
         A., Pajuelo, M., Palacián, J.F., Pallier, G., Paraschiv, P., Pardini, R., Pavone, M., Pavy, G., Payen, G., Pegoraro, A., Peña-Asensio, E., Perez,
330
         L., Pérez-Hoyos, S., Perlerin, V., Peyrot, A., Peth, F., Pic, V., Pietronave, S., Pilger, C., Piquel, M., Pisanu, T., Poppe, M., Portois, L., Prezeau,
         J.F., Pugno, N., Quantin, C., Quitté, G., Rambaux, N., Ravier, E., Repetti, U., Ribas, S., Richard, C., Richard, D., Rigoni, M., Rivet, J.P., Rizzi,
         N., Rochain, S., Rojas, J.F., Romeo, M., Rotaru, M., Rotger, M., Rougier, P., Rousselot, P., Rousset, J., Rousseu, D., Rubiera, O., Rudawska,
         R., Rudelle, J., Ruguet, J.P., Russo, P., Sales, S., Sauzereau, O., Salvati, F., Schieffer, M., Schreiner, D., Scribano, Y., Selvestrel, D., Serra,
         R., Shengold, L., Shuttleworth, A., Smareglia, R., Sohy, S., Soldi, M., Stanga, R., Steinhausser, A., Strafella, F., Sylla Mbaye, S., Smedley,
         A.R., Tagger, M., Tanga, P., Taricco, C., Teng, J.P., Tercu, J.O., Thizy, O., Thomas, J.P., Tombelli, M., Trangosi, R., Tregon, B., Trivero,
         P., Tukkers, A., Turcu, V., Umbriaco, G., Unda-Sanzana, E., Vairetti, R., Valenzuela, M., Valente, G., Varennes, G., Vauclair, S., Vergne,
         J., Verlinden, M., Vidal-Alaiz, M., Vieira-Martins, R., Viel, A., Vîntdevară, D.C., Vinogradoff, V., Volpini, P., Wendling, M., Wilhelm, P.,
         Wohlgemuth, K., Yanguas, P., Zagarella, R., Zollo, A., 2020. FRIPON: A worldwide network to track incoming meteoroids. Astronomy and
         Astrophysics 644, A53. URL: https://www.aanda.org/articles/aa/full_html/2020/12/aa38649-20/aa38649-20.htmlhttps:
         //www.aanda.org/articles/aa/abs/2020/12/aa38649-20/aa38649-20.html,doi:10.1051/0004-6361/202038649.
```

- Dmitriev, V., Lupovka, V., Gritsevich, M., 2015. Orbit determination based on meteor observations using numerical integration of equations of motion. Planetary and Space Science, 223–235URL: http://dx.doi.org/10.1016/j.pss.2015.06.015, doi:10.1016/j.pss.2015.06.015.
- Drew, K., Brown, P.G., Close, S., Durand, D., 2004. Meteoroid bulk density determination using radar head echo observations. Earth, Moon, and Planets 95, 639–645. doi:10.1007/s11038-005-2246-2.
- Dyrud, L.P., Ray, L., Oppenheim, M., Close, S., Denney, K., 2005. Modelling high-power large-aperture radar meteor trails. Journal of Atmospheric and Solar-Terrestrial Physics 67, 1171–1177. URL: https://www.sciencedirect.com/science/article/pii/S1364682605001215, doi:10.1016/j.jastp.2005.06.016.
- Dyrud, L.P., Wilson, D., Boerve, S., Trulsen, J., Pecseli, H., Close, S., Chen, C., Lee, Y., 2008a. Plasma and electromagnetic simulations of meteor head echo radar reflections. Earth, Moon and Planets 102, 383–394. URL: https://link.springer.com/chapter/10.1007/352
   352 978-0-387-78419-9\_54http://link.springer.com/10.1007/s11038-007-9189-8, doi:10.1007/s11038-007-9189-8.
- Dyrud, L.P., Wilson, D., Boerve, S., Trulsen, J., Pecseli, H., Close, S., Chen, C., Lee, Y., 2008b. Plasma and electromagnetic wave simulations of meteors. Advances in Space Research 42, 136–142. URL: https://www.sciencedirect.com/science/article/pii/S0273117707002645?casa\_token=YT04ij5ic-oAAAAA:
  - UFZldurW50PkaE2X2cz8j45mVeeITxFCr57gAqXYGJ3uanrrnFPkZl-gr3u2DYp80PNZdWXaFw, doi:10.1016/j.asr.2007.03.048.
- de la Fuente Marcos, C., de la Fuente Marcos, R., 2013. The chelyabinsk superbolide: A fragment of asteroid 2011 EO40? Monthly Notices of the
  Royal Astronomical Society: Letters 436. doi:10.1093/mnras1/s1t103.
- Granvik, M., Brown, P.G., 2018. Identification of meteorite source regions in the Solar System. Icarus 311, 271–287. URL: https://doi.org/10.1016/j.icarus.2018.04.012, doi:10.1016/j.icarus.2018.04.012.
- Hajduková, M., Kornoš, L., 2020. The influence of meteor measurement errors on the heliocentric orbits of meteoroids. Planetary and Space Science 190. doi:10.1016/j.pss.2020.104965.
- Hajduková, M., Sterken, V., Wiegert, P.A., Kornoš, L., 2020. The challenge of identifying interstellar meteors. Planetary and Space Science 192.
   doi:10.1016/j.pss.2020.105060.
- Hall, T.D., Duff, G.F., Maciel, L.J., 2012. The Space Mission at Kwajalein. Lincoln Laboratory Journal 19.
- Janches, D., Close, S., Fentzke, J.T., 2008. A comparison of detection sensitivity between ALTAIR and Arecibo meteor observations: Can high power and large aperture radars detect low velocity meteor head-echoes. Icarus 193, 105–111. URL: www.elsevier.com/locate/icarus, doi:10.1016/j.icarus.2007.08.022.
- Jansen-Sturgeon, T., Sansom, E.K., Bland, P.A., 2019. Comparing analytical and numerical approaches to meteoroid orbit determination using

#### Meteoroid Orbit Determination from HPLA Radar Data

- Hayabusa telemetry. Meteoritics and Planetary Science 54, 2149-2162. doi:10.1111/maps.13376. 370
- Jansen-Sturgeon, T., Sansom, E.K., Devillepoix, H.A.R., Bland, P.A., Towner, M.C., Howie, R.M., Hartig, B.A.D., 2020. A Dynamic 371 372 Trajectory Fit to Multisensor Fireball Observations. The Astronomical Journal 160, 190. URL: https://iopscience.iop.org/ article/10.3847/1538-3881/abb090https://iopscience.iop.org/article/10.3847/1538-3881/abb090/metahttps: 373
- //ui.adsabs.harvard.edu/abs/2020AJ....160..190J/abstract, doi:10.3847/1538-3881/abb090. 374
- Jenniskens, P., Gural, P.S., Dynneson, L., Grigsby, B.J., Newman, K.E., Borden, M., Koop, M., Holman, D., 2011. CAMS: Cameras for Allsky 375 Meteor Surveillance to establish minor meteor showers, Icarus 216, 40-61, URL; http://dx.doi.org/10.1016/j.icarus.2011.08.012, 376 doi:10.1016/j.icarus.2011.08.012. 377
- Kanamori, T., 2009. A meteor shower catalog based on video observations in 2007-2008. WGN, the Journal of the IMO 37, 55-62. 378
- Kozak, P., 2008. "Falling Star": Software for processing of double-station TV meteor observations. Earth, Moon and Planets 102, 277–283. 379 doi:10.1007/s11038-007-9223-x. 380
- Langbrock, M., 2004. A spreadsheet that calculates meteor orbits. WGN. The Journal of the IMO 32, 109–110. 381
- Li, A., Close, S., 2015. Mean thermospheric density estimation derived from satellite constellations. Advances in Space Research 56, 1645–1657. 382 doi:10.1016/j.asr.2015.07.022. 383
- Li, A., Close, S., 2016. Neutral density estimation derived from meteoroid measurements using high-power, large-aperture radar. Journal of Geo-384 physical Research 121, 8023-8037. URL: https://agupubs.onlinelibrary.wiley.com/doi/full/10.1002/2015JD024547https: 385 //agupubs.onlinelibrary.wiley.com/doi/abs/10.1002/2015JD024547https://agupubs.onlinelibrary.wiley.com/doi/ 386 10.1002/2015JD024547, doi:10.1002/2015JD024547. 387
- Limonta, L., Close, S., Marshall, R.A., 2020. A technique for inferring lower thermospheric neutral density from meteoroid ablation. Planetary and 388 Space Science 180, 104735. doi:10.1016/j.pss.2019.104735. 389
- Loveland, R., MacDonell, A., Close, S., Oppenheim, M., Colestock, P., 2011. Comparison of methods of determining meteoroid range rates from 300 linear frequency modulated chirped pulses. Radio Science 46. doi:10.1029/2010RS004479. 391
- Marshall, R.A., Brown, P., Close, S., 2017. Plasma distributions in meteor head echoes and implications for radar cross section interpretation. 392 Planetary and Space Science 143, 203-208. URL: http://dx.doi.org/10.1016/j.pss.2016.12.011, doi:10.1016/j.pss.2016.12. 303
- Marshall, R.A., Close, S., 2015. An FDTD model of scattering from meteor head plasma. Journal of Geophysical Research A: Space 305 Physics 120, 5931-5942. URL: https://agupubs.onlinelibrary.wiley.com/doi/full/10.1002/2015JA021238https: //agupubs.onlinelibrary.wiley.com/doi/abs/10.1002/2015JA021238https://agupubs.onlinelibrary.wiley.com/doi/ 10.1002/2015JA021238, doi:10.1002/2015JA021238.
- Meisel, D.D., Janches, D., Mathews, J.D., 2002a. Extrasolar Micrometeors Radiating from the Vicinity of the Local Interstellar Bubble. The Astrophysical Journal 567, 323–341. doi:10.1086/322317.
- Meisel, D.D., Janches, D., Mathews, J.D., 2002b. The Size Distribution of Arecibo Interstellar Particles and Its Implications. The Astrophysical Journal 579, 895-904. doi:10.1086/342919.
- Montenbruck, O., Gill, E., 2012. Satellite Orbits. Springer. doi:10.1119/1.2350573.
- Pecina, P., 2016. An analytical theory of radio-wave scattering from meteoric ionization I. Basic equation. Monthly Notices of the Royal Astronomical Society 455, 2200-2206. URL: https://ui.adsabs.harvard.edu/abs/2016MNRAS.455.2200P/abstract, doi:10.1093/ mnras/stv2363.
- Pellinen-Wannberg, A., Wannberg, G., Kero, J., Szasz, C., Westman, A., 2008. The impact of high-resolution radar on meteor studies: The EISCAT perspective. URSI Radio Science Bulletin 324, 17-28. URL: https://ieeexplore.ieee.org/document/7909662.
- Peña-Asensio, E., Trigo-Rodríguez, J.M., Gritsevich, M., Rimola, A., 2021. Accurate 3D fireball trajectory and orbit calculation using the 3D-409 firetoc automatic Python code. Monthly Notices of the Royal Astronomical Society 504, 4829-4840. URL: http://arxiv.org/abs/2103. 410 13758http://dx.doi.org/10.1093/mnras/stab999, doi:10.1093/mnras/stab999. 411
- Southworth, R.B., Hawkins, G.S., 1963. Statistics of meteor streams. Smithsonian Contributions to Astrophysics, 261–285. 412
- Sugar, G., Oppenheim, M.M., Dimant, Y.S., Close, S., 2018. Formation of Plasma Around a Small Meteoroid: Simulation and The-413 Journal of Geophysical Research: Space Physics 123, 4080-4093. URL: https://agupubs.onlinelibrary.wiley.com/ 414 doi/full/10.1002/2018JA025265https://agupubs.onlinelibrary.wiley.com/doi/abs/10.1002/2018JA025265https: 415 //agupubs.onlinelibrary.wiley.com/doi/10.1002/2018JA025265, doi:10.1002/2018JA025265. 416
- Sugar, G., Oppenheim, M.M., Dimant, Y.S., Close, S., 2019. Formation of Plasma Around a Small Meteoroid: Electrostatic Simula-417 Journal of Geophysical Research: Space Physics 124, 3810-3826. URL: https://agupubs.onlinelibrary.wiley.com/ 418 doi/full/10.1029/2018JA026434https://agupubs.onlinelibrary.wiley.com/doi/abs/10.1029/2018JA026434https: 419 420
  - //agupubs.onlinelibrary.wiley.com/doi/10.1029/2018JA026434, doi:10.1029/2018JA026434.
- Trigo-Rodríguez, J.M., 2019. The flux of meteoroids over time: meteor emission spectroscopy and the delivery of volatiles and chondritic materials 421 to Earth, in: Hypersonic Meteoroid Entry Physics. IOP Publishing, pp. 4-1. doi:10.1088/2053-2563/aae894ch4. 422
- Trigo-Rodríguez, J.M., Blum, J., 2022. Learning about comets from the study of mass distributions and fluxes of meteoroid streams. Monthly 423 Notices of the Royal Astronomical Society 512, 2277–2289. doi:10.1093/mnras/stab2827. 424
- Trigo-Rodríguez, J.M., Lyytinen, E., Gritsevich, M., Moreno-Ibáñez, M., Bottke, W.F., Williams, I., Lupovka, V., Dmitriev, V., Kohout, T., 425 Grokhovsky, V., 2015. Orbit and dynamic origin of the recently recovered Annama's H5 chondrite. Monthly Notices of the Royal Astronomical 426 Society 449, 2119-2127. URL: https://academic.oup.com/mnras/article/449/2/2119/1074901, doi:10.1093/mnras/stv378. 427
- Vertatschitsch, L.E., Sahr, J.D., Colestock, P., Close, S., 2011. Meteoroid head echo polarization features studied by numerical electromagnetics 428 modeling. Radio Science 46, 6016. URL: https://agupubs.onlinelibrary.wiley.com/doi/full/10.1029/2011RS004774https: 429 //agupubs.onlinelibrary.wiley.com/doi/abs/10.1029/2011RS004774https://agupubs.onlinelibrary.wiley.com/doi/ 430 10.1029/2011RS004774, doi:10.1029/2011RS004774. 431
- Vida, D., Brown, P.G., Campbell-Brown, M.D., 2018. Modelling the measurement accuracy of pre-atmosphere velocities of meteoroids. Monthly 432

#### Meteoroid Orbit Determination from HPLA Radar Data

- Notices of the Royal Astronomical Society 479, 4307–4319. URL: https://academic.oup.com/mnras/article/479/4/4307/5054048, doi:10.1093/mnras/sty1841.
- Vida, D., Gural, P.S., Brown, P.G., Campbell-Brown, M.D., Wiegert, P., 2020. Estimating trajectories of meteors: An observational Monte Carlo
   approach I. Theory. Monthly Notices of the Royal Astronomical Society 491, 2688–2705. URL: https://academic.oup.com/mnras/
   article-abstract/491/2/2688/5626361, doi:10.1093/mnras/stz3160.
- Volz, R., Close, S., 2012. Inverse filtering of radar signals using compressed sensing with application to meteors. Radio Science 47, 0-05.
   URL: https://agupubs.onlinelibrary.wiley.com/doi/full/10.1029/2011RS004889https://agupubs.onlinelibrary.wiley.com/doi/10.1029/2011RS004889,
   doi:10.1029/2011RS004889.
- Weryk, R.J., Brown, P.G., 2004. A search for interstellar meteoroids using the Canadian Meteor Orbit Radar (CMOR). Earth, Moon and Planets
   95, 221–227. doi:10.1007/s11038-005-9034-x.
- Yee, J., Close, S., 2013. Plasma turbulence of nonspecular trail plasmas as measured by a high-power large-aperture radar. Journal of Geophysical Research Atmospheres 118, 449-13. URL: https://agupubs.pericles-prod.literatumonline.com/doi/full/
  10.1002/2013JD020247https://agupubs.pericles-prod.literatumonline.com/doi/abs/10.1002/2013JD020247https:
  //agupubs.onlinelibrary.wiley.com/doi/10.1002/2013JD020247, doi:10.1002/2013JD020247.
- Zoladek, P., 2011. PyFN multipurpose meteor software, in: Proceedings of the International Meteor Conference, pp. 53–55.
- Zuluaga, J.I., Ferrin, I., Geens, S., 2013. The orbit of the Chelyabinsk event impactor as reconstructed from amateur and public footage. URL:
   https://arxiv.org/abs/1303.1796v1http://arxiv.org/abs/1303.1796.